Supplementary Information for

Thermodynamically reversible paths of the first fusion intermediate reveal an important role for membrane anchors of fusion proteins

Yuliya G. Smirnova, Herre Jelger Risselada, Marcus Müller

Yuliya G. Smirnova.
E-mail: ysmirno@gwdg.de

This PDF file includes:

Supplementary text
Figs. S1 to S11
Table S1
References for SI reference citations

www.pnas.org/cgi/doi/10.1073/pnas.1818200116

Supporting Information Text

Methods. The improved string method (1) consists in iterating two steps: (1) minimize the free energy of the system via Allen-Cahn dynamics (or model A (2)), $\Delta m_s(\mathbf{r}) \sim -\frac{\delta F[m_s]}{\delta m_s(\mathbf{r})}$, and (2) parameterize the morphologies $m_s(\mathbf{r})$ of the transformation path by a cubic spline in the variable s and redistribute the replicas uniformly along the string. This method is well suited to localize saddle-points along the path (3, 4).

In particle-based simulations, the free-energy functional $F[m]$ is unknown and we used field-theoretic umbrella sampling to compute the chemical potential (4–6). To this end, we restrained order-parameter fluctuations by an umbrella potential at each point in space using a collocation grid, see ref. (5), and added this contribution to the Hamiltonian

$$\frac{\Delta H_{\text{umbrella}}(\{\mathbf{r}\})}{k_{\text{B}}T} = \frac{\lambda}{2}\int \mathrm{d}^3\mathbf{r}\,\Big(m_s(\mathbf{r}) - \hat{m}(\mathbf{r}|\{\mathbf{r}\})\Big)^2 \qquad \text{[S1]}$$

where $\hat{m}(\mathbf{r}|\{\mathbf{r}\})$ denotes the order-parameter that is computed from the explicit coordinates, $\{\mathbf{r}\}$, of the particle configuration. In the large-force-constant-λ limit, we compute the chemical potential according to

$$\mu_s(\mathbf{r}) = \frac{\delta F}{\delta m_s(\mathbf{r})} \approx k_{\text{B}}T\lambda\left[m_s(\mathbf{r}) - \langle\hat{m}(\mathbf{r}|\{\mathbf{r}\})\rangle_{\text{umbrella}}\right] \qquad \text{[S2]}$$

As the order-parameter we used the hydrophobic number density of lipid tail beads for pure POPC and POPE membranes, and POPC membranes with transmembrane peptides. The local microscopic density is a function of the explicit particle coordinates:

$$\hat{m}(\mathbf{r}|\{\mathbf{r}\}) = \sum_{i_H}\delta(\mathbf{r}_{i_H} - \mathbf{r}), \qquad \text{[S3]}$$

where index i_H runs over all hydrophobic tail beads of lipid molecules. In simulations the order-parameter is evaluated by assigning the particle coordinates onto a collocation lattice with the unit cell volume, ΔL^3, and calculating the instantaneous density in each grid cell, $\mathbf{c}$, according to

$$\hat{m}(\mathbf{c}) = \int_V \frac{\mathrm{d}\mathbf{r}}{\Delta L^3}\,W(\mathbf{r},\mathbf{c})\,\hat{m}(\mathbf{r}|\{\mathbf{r}\}) = \frac{1}{\Delta L^3}\sum_{i_H} W(\mathbf{r}_{i_H},\mathbf{c}) \qquad \text{[S4]}$$

where the integration is over the system volume V. We used the following linear assignment function:

$$W(\mathbf{r}_{i_H},\mathbf{c}) = \prod_{\alpha\in\{x,y,z\}} w_\alpha(|\mathbf{r}_{i_H\alpha} - \mathbf{r}_{\mathbf{c}\alpha}|), \qquad \text{[S5]}$$

$$w_\alpha(|\Delta\mathbf{r}_\alpha|) = \begin{cases} 1 - \frac{|\Delta\mathbf{r}_\alpha|}{\Delta L_\alpha} & \text{if } |\Delta\mathbf{r}_\alpha| \le \Delta L_\alpha \\ 0 & \text{otherwise.} \end{cases} \qquad \text{[S6]}$$

where $\mathbf{r}_\mathbf{c}$ denotes the position of cell $\mathbf{c}$, and the unit cell volume is $\Delta L^3 = \Delta L_x \Delta L_y \Delta L_z$. The weight function, $W(\mathbf{r}_{i_H},\mathbf{c})$, has the following properties: $\sum_\mathbf{c} W(\mathbf{r}_{i_H},\mathbf{c}) = 1$ for any $\mathbf{r}_{i_H}$ and $\int_V \mathrm{d}\mathbf{r}\,W(\mathbf{r},\mathbf{c}) = \Delta L^3$ for any grid point $\mathbf{c}$. The first condition ensures that the total number of particles in the system is conserved and the second condition indicates that the volume of each grid cell, i.e., the volume over which each particle is smeared out, is ΔL^3. The assignment function must be differentiable for the calculation of forces acting on particles in the field-theoretic umbrella potential.

The free-energy profile along the Minimum-Free-Energy-Path (MFEP) or string, $m_s(\mathbf{r})$, is obtained via thermodynamic integration of the chemical potential μ_s along the path.

$$\begin{aligned} \Delta F(s) &= \int_0^s \mathrm{d}s'\,\frac{\mathrm{d}F}{\mathrm{d}s'}, \\ \frac{\mathrm{d}F}{\mathrm{d}s} &= \int \mathrm{d}^3\mathbf{r}\,\frac{\delta F[m_s]}{\delta m_s(\mathbf{r})}\,\frac{\mathrm{d}m_s(\mathbf{r})}{\mathrm{d}s} = \int \mathrm{d}^3\mathbf{r}\,\mu_s(\mathbf{r})\frac{\mathrm{d}m_s(\mathbf{r})}{\mathrm{d}s} \end{aligned} \qquad \text{[S7]}$$

The chemical potential for each structure s is obtained as the small difference between the density distribution, $m_s(\mathbf{r})$, for which we calculate the chemical potential, and the average density distribution $\langle\hat{m}(\mathbf{r}|\{\mathbf{r}\})\rangle_{\text{umbrella}}$, which we obtain in the simulation with the field-theoretic umbrella potential. The measurement of μ_s is a computational challenge. In the simulation, μ_s is obtained from a finite-time average of $\langle\hat{m}(\mathbf{r}|\{\mathbf{r}\})\rangle_{\text{umbrella}}$. Therefore each measurement exhibits a finite statistical error.

Since the calculation of the free-energy profile, $\Delta F(s)$, according to Eq. (S7) involves $\mu_s(\mathbf{r})$, the statistical error of the measurement of the chemical potential gives rise to a statistical error of the free-energy profile. These are the deviations observed in Fig. S1. Note that the statistical error is rather large because it involves the chemical potential at each (discrete) point in space, i.e., the free energy, F, is an extensive quantity whereas the free-energy difference between two apposing membranes and a stalk is independent from the lateral extension of the membrane.

After the MFEP itself has converged, i.e., $\frac{\mathrm{d}m_s(\mathbf{r})}{\mathrm{d}s}$ remains unaltered by the updates of the string, the equations above demonstrate that averaging over different measurements of $\Delta F(s)$ is equivalent to extending the simulation time used to obtain the average $\langle\hat{m}(\mathbf{r}|\{\mathbf{r}\})\rangle_{\text{umbrella}}$ for the calculation of μ_s. Therefore we average $\Delta F(s)$ over the last updates of the string.

The number of points for the density-on-the-grid calculation was 20 per each dimension and the force constant $\lambda = 50$ kJ mol^{-1} nm^{-2} (Gromacs units). The string convergence, using Allen-Cahn dynamics and Euler integration scheme, required 200-300 updates each of the length 100-150 ns. For the final results we plotted free-energy profiles averaged over the last 50 updates. Standard deviations were estimated from the plateau values of the free-energy barrier and the stalk free energy, see Fig. S1.

For the calculations of the difference between the excess free energies of the stalk structure in different systems, e.g. POPE and POPC membranes as well as POPC membranes with and without SNARE transmembrane peptides, we used the thermodynamic integration method (7). The non-bonded interactions in the system Hamiltonian were presented as, $H(\lambda) = (1-\lambda)H_A + \lambda H_B$, with the parameter $0 \leq \lambda \leq 1$. Here H_A corresponds to the system with non-bonded interactions of PE lipids or non-bonded interactions of the system with SNARE transmembrane peptides, e.g. $\lambda = 0$ systems. H_B corresponds to the system with non-bonded interactions of PC lipids or the system with SNARE transmembrane peptides which have zero non-bonded interactions with other particles in the system, e.g. $\lambda = 1$ systems. The free-energy difference between two states corresponding to $\lambda = 0$ and $\lambda = 1$, was obtained by integrating the equation numerically

$$\Delta F = F_{\lambda=1} - F_{\lambda=0} = \int \mathrm{d}\lambda \, \frac{\mathrm{d}F}{\mathrm{d}\lambda} = \int \mathrm{d}\lambda \left\langle \frac{\partial H(\{\mathbf{r}\},\lambda)}{\partial \lambda} \right\rangle_\lambda . \qquad [S8]$$

Free-energy convergence. In simulations the path updates were performed according to the improved and simplified string method of Vanden-Eijnden, E, and Ren (1), i.e., after computing the chemical potential, $\mu(\mathbf{c})$, for each point $\mathbf{c}$ on the collocation grid, we locally minimize the free energy according to

$$m(\mathbf{c})_n = m(\mathbf{c})_{n-1} - \frac{\mu(\mathbf{c})}{kT}\,\Delta t, \qquad [S9]$$

were $m(\mathbf{c})_n$ and $m(\mathbf{c})_{n-1}$ denote the new and the current density field (order parameter), respectively. Δt is a small parameter that corresponds to the (dimensionless) "time" step of the Euler integration of the Allen-Cahn equation. Subsequently, the points along the string are uniformly distributed along the string using a pointwise spline.

From the last path (string) updates, see Fig. S1, the mean values of the free-energy barrier and the stalk free energy with respect to the bilayer state, as well as the standard deviations were estimated and compared to the plateau value from the exponential fit of the free-energy values with respect to the number, n, of string updates.

The exponential fit is only used to illustrate the convergence of the string towards MFEP, in particular the barrier and stalk free-energy differences, as a function of the number of string updates. The functional form assumes that in the vicinity of the MFEP the valley on the free-energy landscape has a finite, positive curvature in the direction perpendicular to the MFEP. The fit allows us to estimate the plateau values of the two free-energy differences and provides a crude estimate for the convergence time of the string.

Minimum free-energy paths for membranes under tension. Our simulations for the free-energy calculations were performed in the canonical NVT ensemble. Although the membranes can adjust the area to the given hydration level and have zero membrane tension, their leaflets have different solvation conditions: low hydration in the direction of the neighboring membrane (*cis* leaflets) and full hydration in the opposite direction (*trans* leaflets). Lipid flip-flop is very rear event and may not spontaneously occur even in very long simulations. Therefore, the leaflets are under some tension (negative for the *trans* (distal) leaflets and positive for the *cis* (apposed) monolayers). This may give additional contribution to the free energies. To address this issue we calculated MFEPs for the POPC system with $d_w = 1.2$ nm by performing four sets of simulations with different tensions in the interval 15 – 40 mN/m per each membrane. The applied tension resulted in an expected reduction of the intermembrane distance in the canonical ensemble. However, we did not obtain significantly different free-energy profiles for systems under tension but otherwise with similar intermembrane distances, see Fig. S2.

Committor probability analysis. Fig. S3 presents the MFEP for two POPC membranes separated at distance $d_w = 1.01$ nm. The excess free energy of the stalk structure approaches zero. We performed a committor probability analysis in order to localize the transition state and to verify that it corresponds to the free-energy barrier. For this we selected multiple order-parameter configurations around the transition state, typically 6-8 order-parameter configurations in the interval $0.39 \leq s \leq 0.5$ along the string. We generated an ensemble of 200-500 microscopic particle configurations for each order-parameter configuration by simulating the Martini model subjected to the field-theoretic umbrella potential, using the order-parameter configuration as reference for the field-theoretic umbrella potential. For each of these microscopic particle configurations we started unrestrained simulations and count how many of the trajectories converged to the bilayers state or the stalk state. The length of each unrestrained trajectory in the committor analysis methods was 500 ns. This length is long enough such that the system clearly relaxes either to the bilayer or stalk state and remains there. The stalk state was defined as having hydrophobic beads in the space between the bilayers. Based on this we estimated the committor probability to convert into the bilayers state, see Fig. S3. The value of the probability $p = 0.5$ corresponds to the transition state (or a symmetric barrier). We performed the committor analysis also for the 4-times larger system to address the finite-size effects. We superimposed the barrier configurations resolved for the small reference system on part of a 4-times larger system and obtained similar committor probabilities, see Fig. S3, indicating that the barriers in both systems share a similar structure in high dimensional density space, despite a difference in allowed thermal membrane fluctuations.

System configurations close to the transition state correspond to the splayed-lipid-bond ($\sim$ 66%), as well as other configurations, see Fig. S3. From the individual snapshots that belong to the ensemble of microscopic configurations corresponding to the transition state, it is not always easy to see how the membranes deform but the order parameter provides clear information about the evolution of the membrane shape along the MFEP. For example, the transition state corresponds to the deformed membranes where the hydrophobic defects from both membranes (dimples) become connected. The here-observed dimple-like protrusions – which are only visible in the time averaged density – resemble the pre-stalk membrane defects predicted by the continuum elastic model (8).

Hydration repulsion at short intermembrane distances. In order to obtain the hydration repulsion free energies, which are required to bring the membranes to close apposition, we used the same simulation protocol as described in ref. (9), i.e., the distance between the membranes was controlled by using an umbrella potential, acting on lipid tail beads. Small pores in the middle of each membrane were introduced in order to allow solvent to pass through the membranes. The tension-free membranes were simulated in the NPT ensemble. We compared the MFEPs for pure POPC and POPE membranes as well as for membranes under tension (each membrane has tension 25 mN/m), see Fig. S4. The free energy per membrane area is much larger for POPC membranes, because of the larger head group hydration shell compared to POPE lipids. Membrane tension decreases the free-energy cost since membrane interfaces become more hydrophobic. This effect is, however, rather small for reasonable membrane tensions.

Configurational changes of TMDs along the transformation path. Configurational changes of the TMDs along the MFEP are accompanied by changes in the end-to-end distance, see Fig. S5, and the tilt angle, i.e., the angle between the end-to-end vector of the peptide and the bilayer normal, z, see Fig. S6. On average, the peptide end-to-end vector orients in the direction of the stalk center. From these simulations, the lateral distance between the peptide's center of mass and the stalk center is 2 ± 0.1 nm, and the averaged tilt angle amounts to 15 ± 2 degrees. The tilt angle of the transmembrane peptides with respect to the membrane normal has been reported in the broad range of 15 – 55 degrees (10–12).

Stalk structure. The averaged hydrophobic-density profiles of the stalk structures are shown in Fig. S7. The top panel corresponds to the stalk structures formed at different hydration levels, equilibrated in the NPT ensemble without a field-theoretic umbrella potential. For comparison large systems (four times larger than the reference system) with $d_w = 1.2$, $d_w = 1.1$ and $d_w = 1.0$ nm were additionally simulated and the density profile is shown for one large system with $d_w = 1.2$ nm. The bottom panel depicts the corresponding stalk structures, obtained in the field-theoretic umbrella potential in the NVT ensemble, after the MFEP is converged. (We performed the free-energy calculations only with the small system sizes). Overall the structures on the top and bottom panel look similar. The finite-size effects can be seen by comparing the stalk structure on the left and right hand side of the top panel. Large systems have more lipids, and the stalk radius can increase as the structure relaxes. For distances, $d_w < 1.1$ nm, the stalk has a tendency to elongate, which is particularly noticeable for large systems, see acylindricity parameter in Fig. S8. This specifies that the free energy of the stalk structure decreases and indicates the propensity of the system to transit into the inverted hexagonal phase. At the distance around the stalk radius, there is a slight decrease of the membrane thickness around the stalk base, indicating packing frustrations, see arrows in Fig. S7. Another region of packing frustrations is in the middle of the stalk, along the z axis, which also has decreased thickness and density. Packing frustrations in these regions were also observed in earlier simulations (13–15) and experiments (16).

Stalk-TMDs complex. It is interesting to note that the position and orientation of the transmembrane domains closely correlates with the region of membrane thinning around the stalk base, see Fig. S7. By partitioning in the region of large packing frustration peptides lower the excess free energy of the highly bent stalk structure. In the coarse-grained model used in our simulations peptides cannot change their secondary structures, e.g. develop a kink in the α–helices. Nevertheless, our simulations can be used in a good, first approximation, when the peptide's secondary structure does not dramatically change.

From unbiased equilibrium simulations of large systems (four times larger system with two peptides) in the NPT ensemble we also observed that the peptides and the stalk structure attract each other, having a preferred distance between their centers of 1.8 ± 0.3 nm and an average tilt angle of 18 ± 3 degrees. To investigate the effect of the TMD on the membrane properties, we performed simulations of two systems, each containing one fully hydrated membrane with 512 lipid molecules and 5308 solvent beads, and one transmembrane peptide, syntaxin (syx) or synaptobrevin (syb), respectively. The peptides were inserted at $r = 0$ and thinned the membrane, in agreement with the previous results (17), see Fig. S10. The decay length of the membrane density profile due to the TMD is 0.5 ± 0.1 nm. This decay length is obtained by fitting a single-exponential decay to the density profiles for $r > 1$ nm (the excluded volume effects of the peptides play a role for smaller radii, see black-dashed line in Fig. S10). The average tilt angle for the TMD is about 15 ± 6 degrees, 10 ± 6 for synaptobrevin and 20 ± 6 for syntaxin.

Noticing that both TMDs perturb the hydrophobic core of the membrane, which results in membrane thinning, we performed simulations with an external potential, mimicking the local thinning effect of the peptides. We used an external harmonic potential (18), that acts on the lipid tails, with different radii in the range 0.5–1.0 nm and a force constant 50 kJ mol^{-1} nm^{-2} (Gromacs units). In these simulations we also observed that the stalk and the locally thinned membrane region attract each other and that the preferred distance between the stalk and the perturbed region is 2 nm, see Fig. S11. The larger the radius of the local membrane thinning is, the narrower the distance distribution. This finding is in agreement with previous simulations (13, 19–22), demonstrating attractions of stalks and membrane pores due to the reduction of the line tension of the pore i.e., a reduction in the bending free energy of the stalk-pore complex.

Free-energy calculation – summary. The free-energy results are summarized in Table S1 for all simulated systems: POPC and POPE membranes, POPC membranes with transmembrane domains (syntaxin and synaptobrevin peptides) – TMDs, and POPC membranes under tension: 40, 35, 25 and 15 mN/m per membrane. The number of solvent beads and corresponding intermembrane distances as well as the distances between the centers of mass of the membranes are compiled for each system. The free-energy barrier is denoted by ΔF^*, the excess free energy of the meta-stable stalk structure is ΔF_{st}, obtained from the MFEP calculation using the string method. From the thermodynamic integration method (TI), the free-energy difference is $\Delta\Delta F_{st} = \Delta F_{st}(\mathrm{P}C) - \Delta F_{st}(\mathrm{P}E)$, where $\Delta F_{st}(\mathrm{P}C)$ and $\Delta F_{st}(\mathrm{P}E)$ are the excess free energies of the stalk structure in POPC and POPE systems respectively. As well as $\Delta\Delta F_{st} = \Delta F_{st}(\mathrm{P}C) - \Delta F_{st}(\mathrm{P}C + TMDs)$, where $\Delta F_{st}(\mathrm{P}C)$ and $\Delta F_{st}(\mathrm{P}C + TMDs)$ are the excess free energies of the stalk structure in POPC and POPC with transmembrane peptides (TMDs) respectively. All errors are standard deviations.

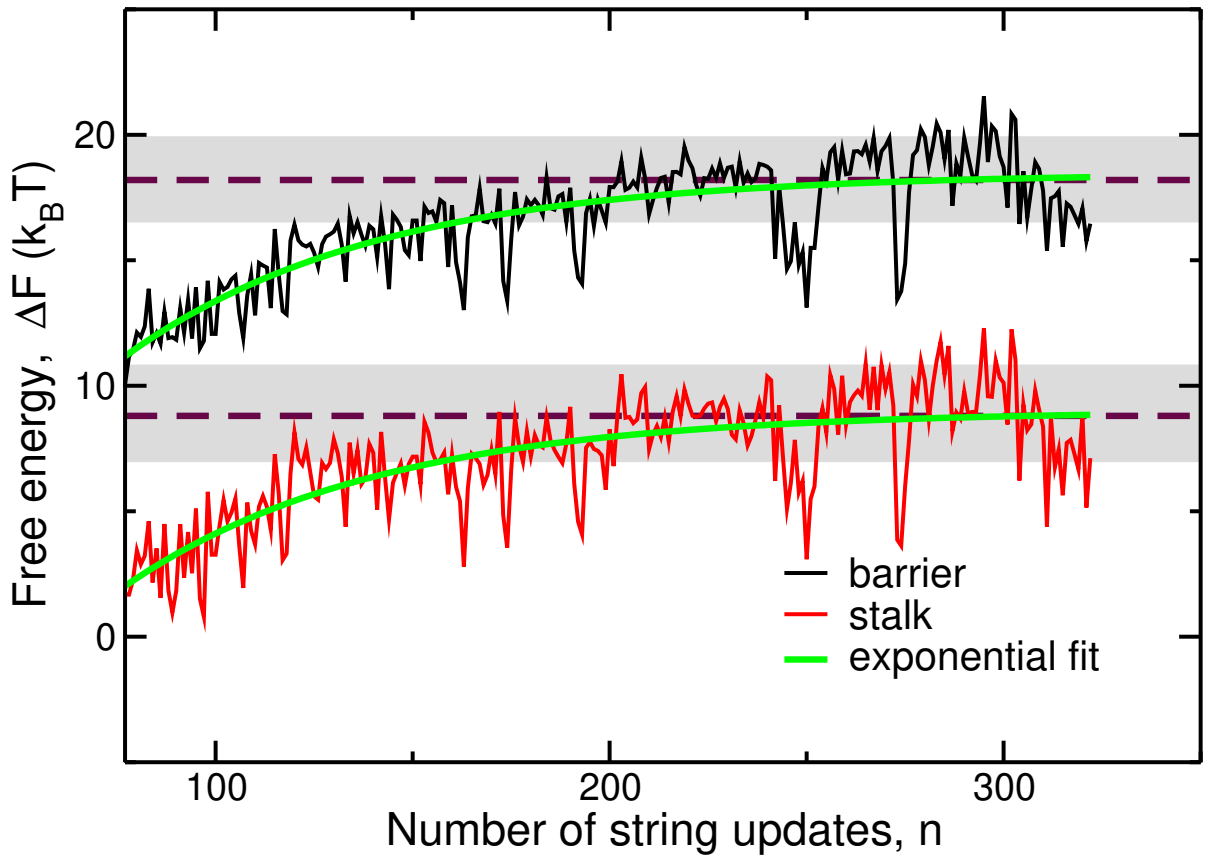

Fig. S1. Free-energy barrier (black) and stalk free energy (red) $versus$ the number of the string updates, n, for the system with intermembrane distance $d_w = 1.09$ nm (PChd180). The exponential fit (green), $\Delta F = a + b\exp(-n/\tau)$, was performed skipping a few points at the beginning. The plateau value, a, is $18.5 \pm 0.5\ k_BT$ and $9.0 \pm 0.5\ k_BT$ for the barrier and the stalk, respectively. The convergence time τ is about 60 string updates. The final free-energy values and standard deviations are depicted by horizontal dashed lines and gray-shaded areas.

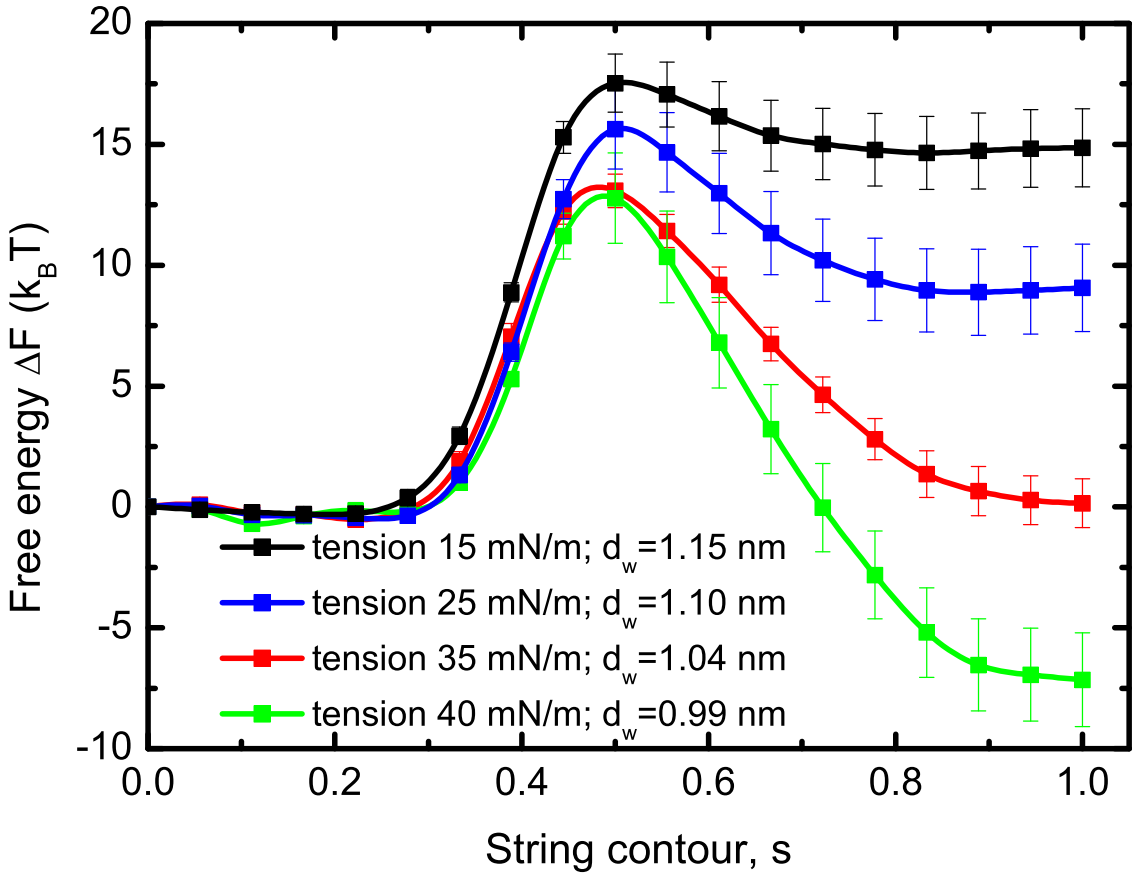

Fig. S2. MFEP for POPC systems under tension: 15 – black ($d_w = 1.15$ nm), 25 – blue ($d_w = 1.10$ nm), 35 – red ($d_w = 1.04$ nm), and 40 mN/m – green ($d_w = 0.99$ nm). Standard deviations are shown with bars.

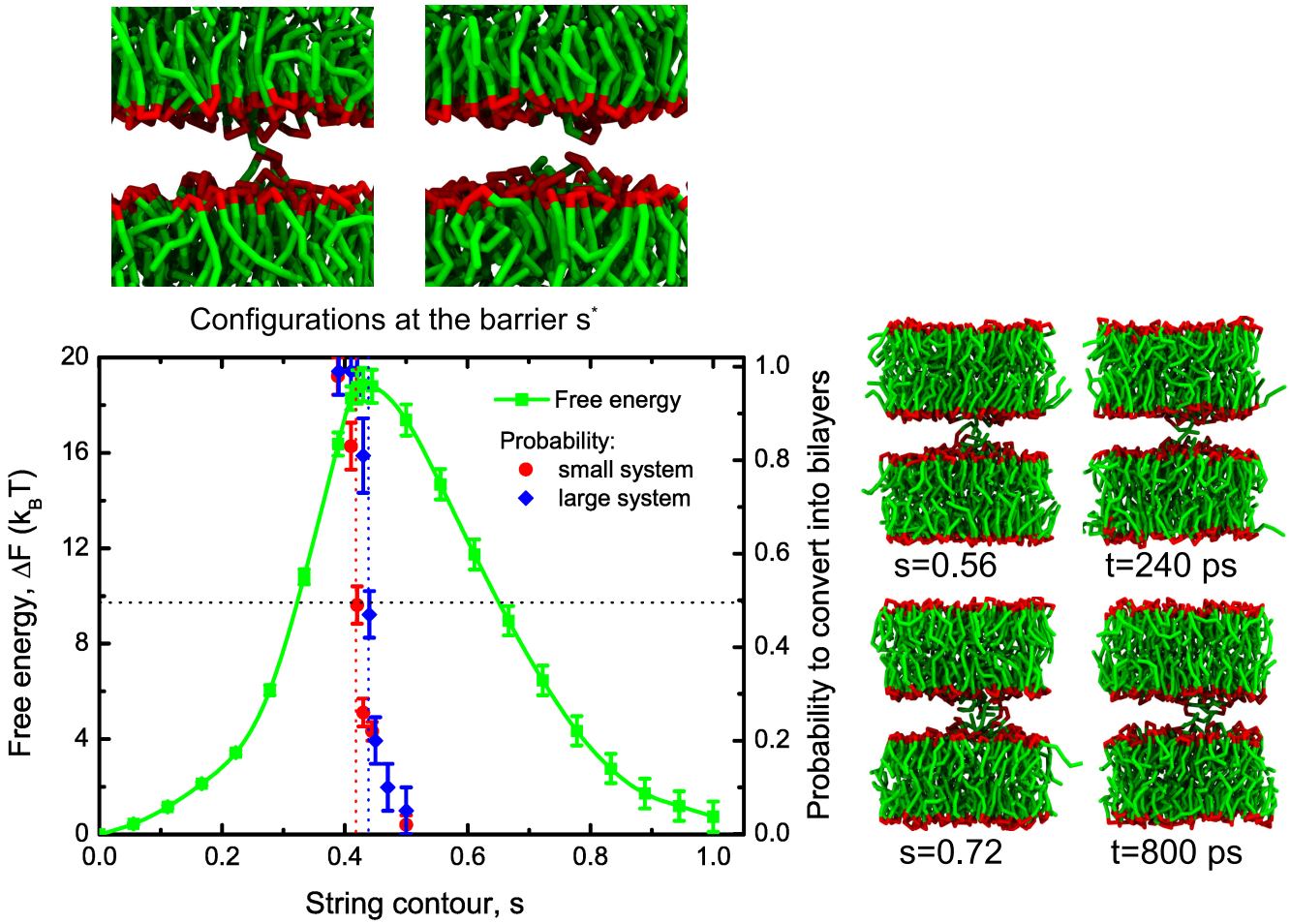

Fig. S3. MFEP for the POPC system with intermembrane distance $d_w = 1.01$ nm (PChd160) – green curve, and committor probability to convert to the lamellar state (non-connected bilayers) – red (reference system) and blue (4-times larger system) points; bars represent standard deviations. The right panel shows two snapshots along the path and two closely corresponding snapshots from the committor probability simulations. The top panel shows two representative configurations around the barrier zoomed in around lipid protrusions. Color code: glycerol backbone – red, lipid tails – green.

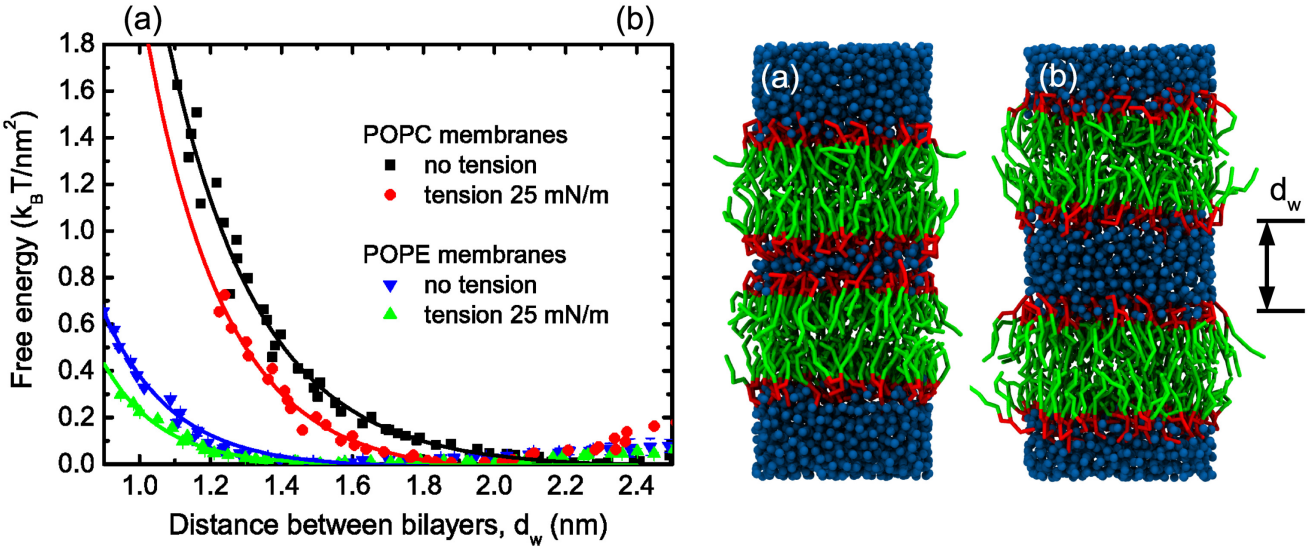

Fig. S4. Free energy of dehydration per membrane area for POPC and POPE membranes with and without membrane tension. Symbols are simulation data and lines are single-exponential decay fits. On the right hand side, the two snapshots of the POPC system correspond to low (a) and high (b) hydration level, respectively. Color code: lipid tails – green, glycerol backbone and polar head groups – red, solvent – blue.

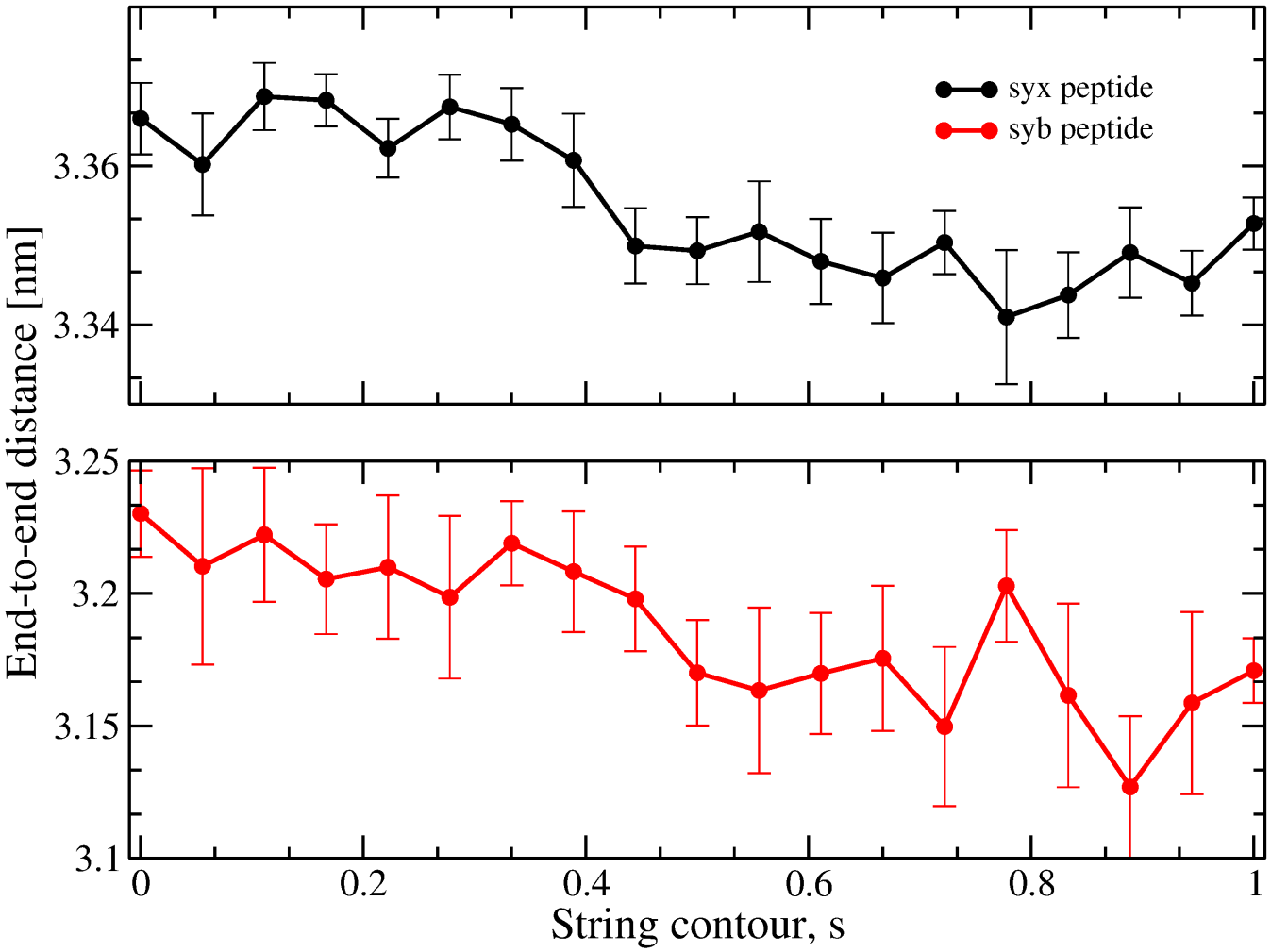

Fig. S5. The end-to-end distance of syntaxin (syx – black) and synaptobrevin (syb – red) transmembrane peptides along the MFEP from the two-bilayers state, $s = 0$, to the stalk state, $s = 1$. Bars represent standard deviations.

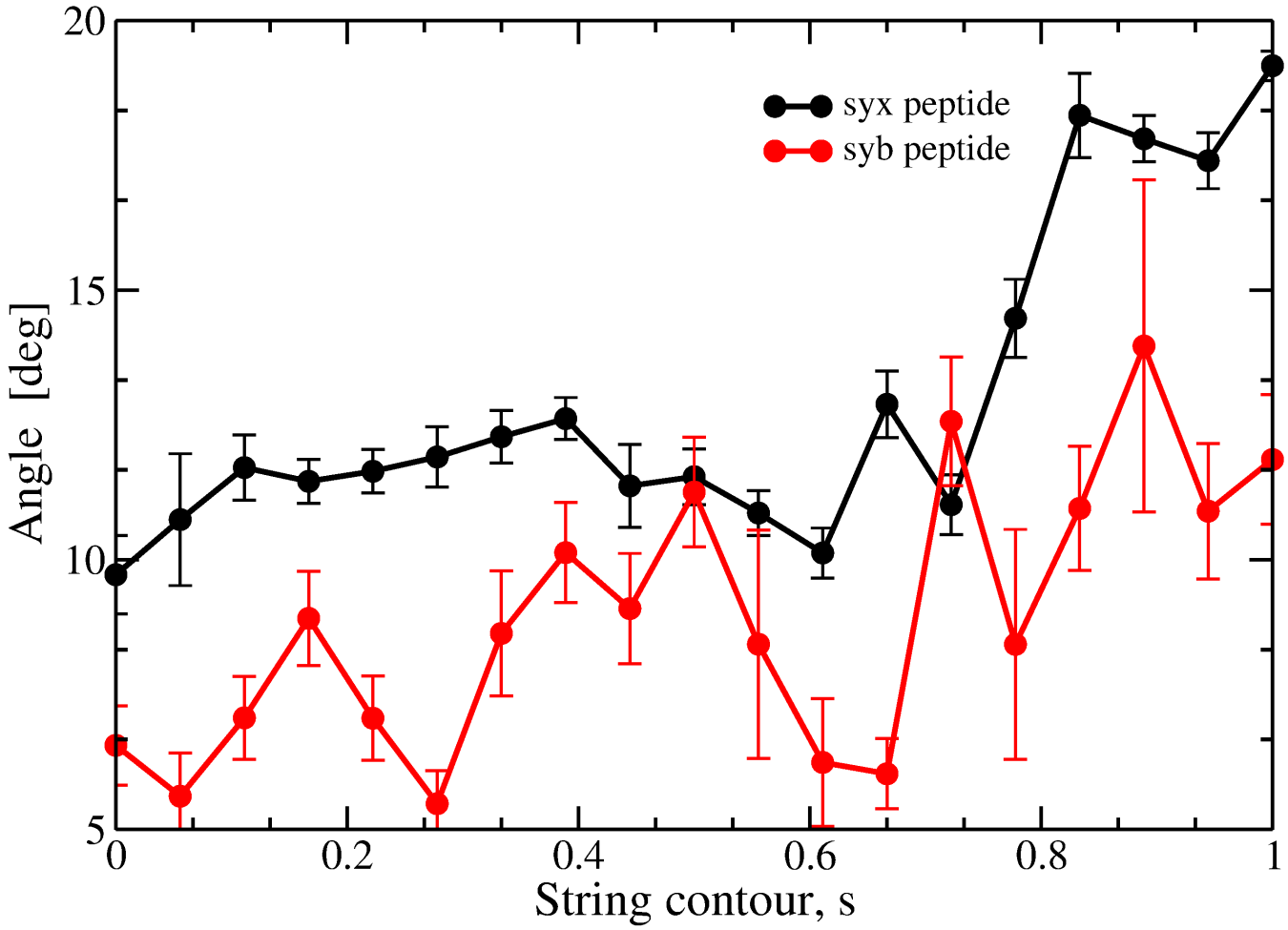

Fig. S6. The tilt angle in degrees (the angle between the peptide's end-to-end vector and the membrane normal, z) along the MFEP for both transmembrane peptides, syntaxin (syx – black) and synaptobrevin (syb – red), respectively. Bars represent standard deviations.

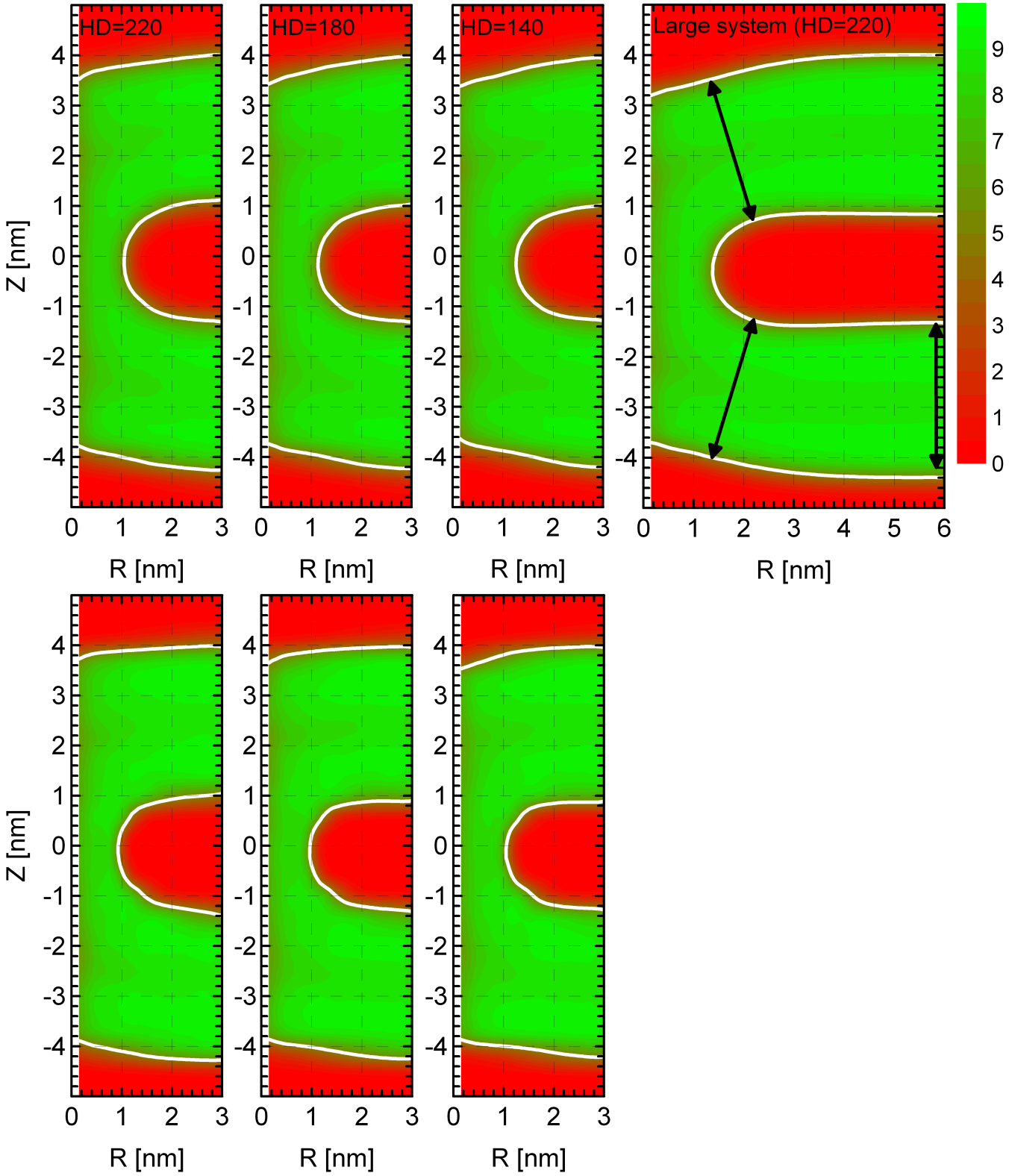

Fig. S7. The hydrophobic number densities (nm^{-3}) for different hydration levels are shown in polar coordinates on rz plane. The structures are averaged with respect to the polar angle, and the axial symmetry axis of the stalk structure coincides with the z axis. The structures on the top correspond to the equilibrium simulations in the NPT ensemble, and the structures below are those obtained after the convergence of the MFEP in the NVT ensemble. The contour level corresponding to the half of the maximal density, is indicated with white color in all plots. The arrows depict the regions of membrane thinning around the stalk base, the same arrow, away from the stalk base, illustrates the membrane thinning as compared to the unperturbed bilayer.

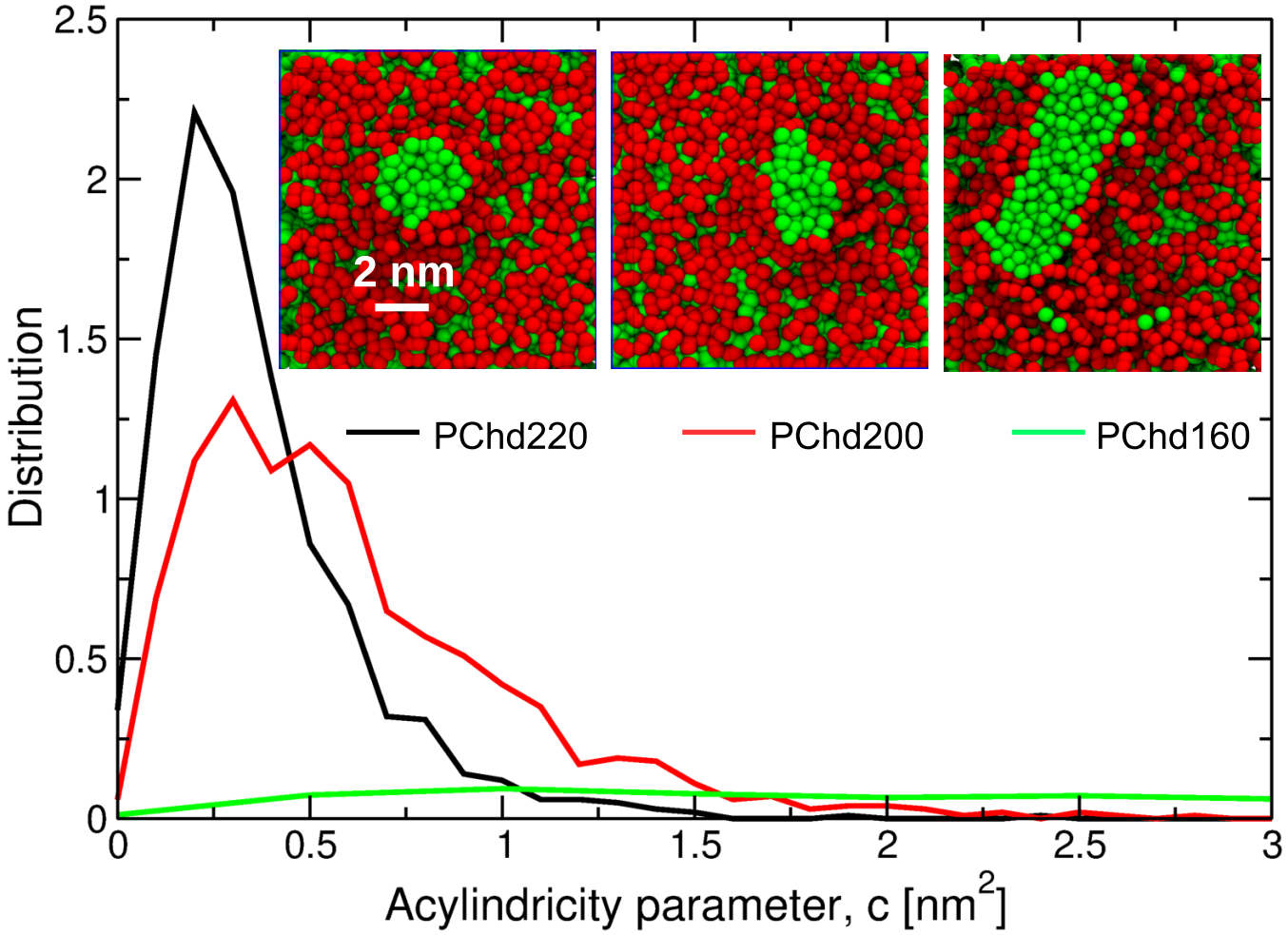

Fig. S8. Acylindricity parameter for three pure lipid systems: PChd220 (black), PChd200 (red), and PChd160 (green). The deviation from circular cross-section of the stalk (acylindricity parameter) is equal to $\lambda_1^2 - \lambda_2^2$, where $\lambda_1 > \lambda_2$ are the two eigenvalues of the 2D gyration tensor. We used a 0.3 nm thin slab along z axis through the middle of the stalk to calculate the gyration tensor in the xy-plane. Only hydrophobic beads were included. The corresponding snapshots depict the half of the systems projected on xy-plane, glycerol backbone – red beads, lipid tails – green beads, and the stalk corresponds to the area of green beads on the snapshots.

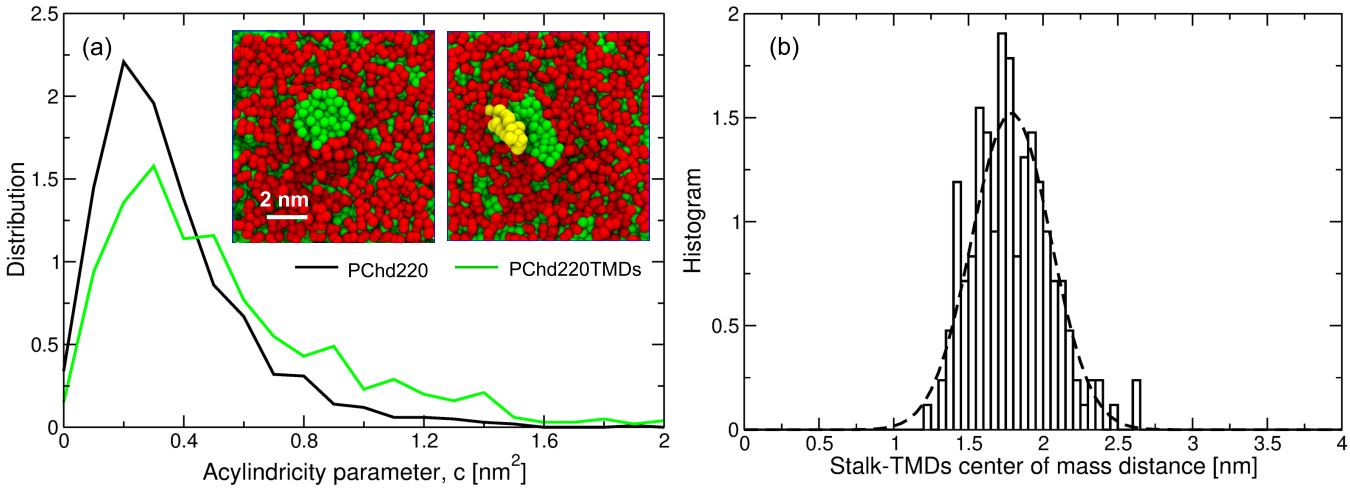

Fig. S9. (a) Acylindricity parameter for two systems: pure lipid system – PChd220, and system with TMDs – PChd220TMDs. The deviation from circular cross-section of the stalk (acylindricity parameter) is equal to $\lambda_1^2 - \lambda_2^2$, where $\lambda_1 > \lambda_2$ are the two eigenvalues of the 2D gyration tensor. We used a 0.3 nm thin slab along z axis through the middle of the stalk to calculate the gyration tensor in the xy-plane. Only hydrophobic beads were included. The snapshots depict the half of the systems projected on xy-plane, glycerol backbone – red beads, lipid tails – green beads, TMDs – yellow beads, and the stalk corresponds to the area of green beads on the snapshots. (b) Histogram of the distance between the center of the mass of the stalk and TMDs on xy-plane. The trajectory length was 1 μs and the first 200 ns were used for equilibration. The Gaussian fit is shown with dashed line. The preferred distance is 1.8 ± 0.3 nm.

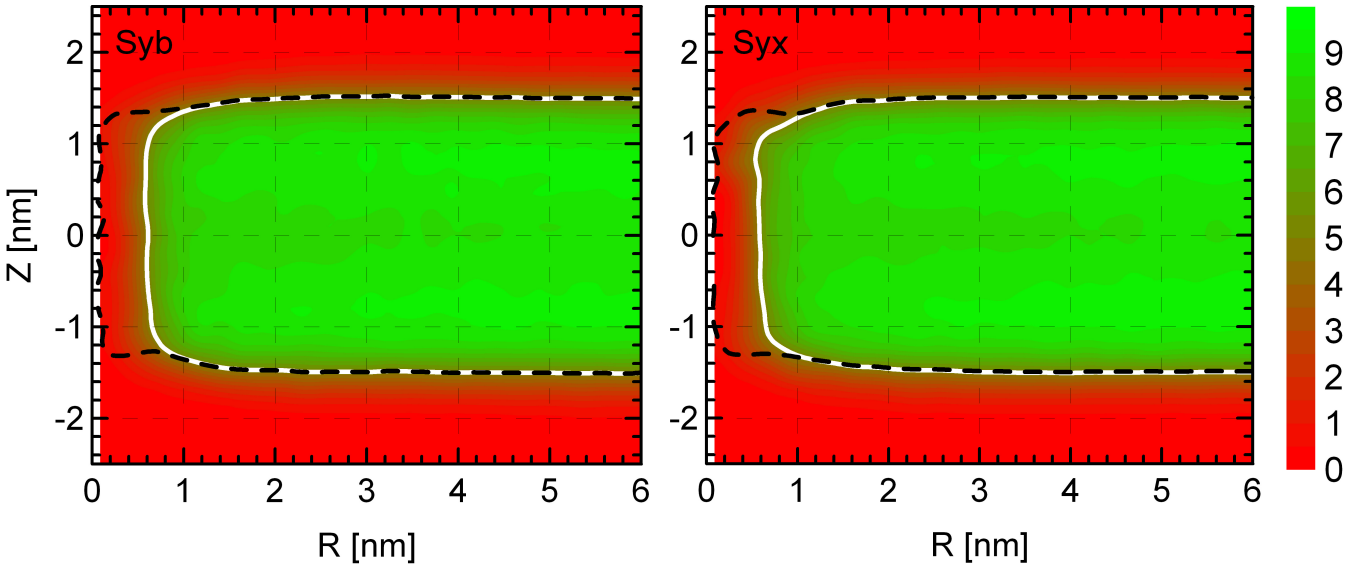

Fig. S10. The hydrophobic number density of lipids (nm^{-3}) are shown. Each peptide, syntaxin (syb) and synaptobrevin (syx), was inserted in one fully hydrated bilayer. In both cases, the center of mass of the peptide corresponds to the origin of the polar coordinate system, and the densities were averaged over the polar angle. The contour level corresponding to the half of the maximal density is shown by the white line, and the black-dashed line depicts the location of the half of the maximal total density (hydrophobic tails and transmembrane domains).

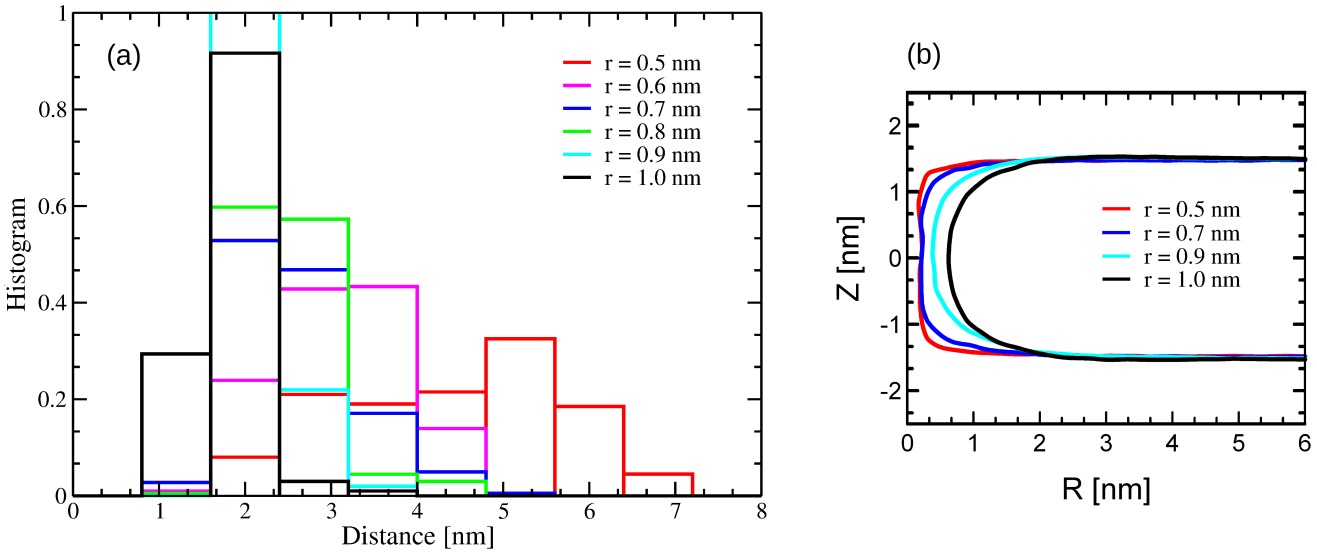

Fig. S11. (a) The histogram of the distances between the center of mass of the stalk and the center of the external harmonic potential, acting on lipid tail beads, with different radii. The external potential introduces membrane thinning for smaller radii and a membrane pore for $r \gtrsim 1$ nm. (b) The number density profiles of the membrane structures with the external potential of different radii. The contour level corresponds to the half of the maximal density.

Table S1. Simulated systems for the free-energy calculations

System	# water beads	d_w (nm)	d_{com} (nm)	ΔF^* (k_BT)	ΔF_{st} (string) (k_BT)	$\Delta\Delta F_{st}$ (TI) (k_BT)
POPC	140	1.00 ± 0.01	5.0 ± 0.01	16.6 ± 0.7	-4.6 ± 1.5	
	160	1.01 ± 0.01	5.0 ± 0.01	19.6 ± 0.8	1.9 ± 1.2	
	180	1.09 ± 0.01	5.07 ± 0.01	18.2 ± 1.8	8.8 ± 1.9	
	200	1.13 ± 0.01	5.11 ± 0.01	19.7 ± 1.0	15.2 ± 1.0	
	220	1.20 ± 0.01	5.14 ± 0.01	23.1 ± 1.0	21.5 ± 1.0	
POPC+tension	220	0.99 ± 0.01	4.58 ± 0.01	15.4 ± 2.6	-3.7 ± 2.6	
	220	1.04 ± 0.01	4.72 ± 0.01	16.6 ± 0.5	4.2 ± 0.9	
	220	1.10 ± 0.01	4.87 ± 0.01	16.1 ± 1.7	9.3 ± 1.8	
	220	1.15 ± 0.01	5.04 ± 0.01	17.8 ± 1.2	14.9 ± 1.5	
POPE	180	1.06 ± 0.01	5.09 ± 0.01	19.8 ± 0.8	7.8 ± 0.9	2 ± 1
POPC+TMDs	220	1.16 ± 0.01	5.08 ± 0.01	14.7 ± 1.2	6.1 ± 2.5	12 ± 1

References

1. W. E, W. Ren, and E. Vanden-Eijnden. Simplified and improved string method for computing the minimum energy paths in barrier-crossing events. *J. Chem. Phys.*, 126:164103, 2007.
2. B. I. Halperin and P. C. Hohenberg. Theory of dynamical critical phenomena. *Rev. Mod. Phys*, 49:435–479, 1977.
3. C. L. Ting, D. Appelö, and Z.G. Wang. Minimum energy path to membrane pore formation and rupture. *Phys. Rev. Lett.*, 106:168101, 2011.
4. M. Müller, Y.G. Smirnova, G. Marelli, M. Fuhrmans, and A. C. Shi. Transition path from two apposed membranes to a stalk obtained by a combination of particle simulations and string method. *Phys. Rev. Lett.*, 108:228103, 2012.
5. Y. G. Smirnova and M. Müller. Calculation of membrane bending rigidity using field-theoretic umbrella sampling. *J. Chem. Phys.*, 143:243155, 2015.
6. Y. G. Smirnova, M. Fuhrmans, I. A. Barragan Vidal, and M. Müller. Free-energy calculation methods for collective phenomena in membranes. *J. Phys. D: Appl. Phys.*, 48:343001, 2015.
7. H.J.C. Berendsen. *Simulating the Physical World.* Cambridge University Press, Cambridge, 2007.
8. A. Efrat, L.V. Chernomordik, and M.M. Kozlov. Point-like protrusion as a prestalk intermediate in membrane fusion pathway. *Biophys. J.*, 92:L61–L63, 2007.
9. Y. G. Smirnova, S. Aeffner, H. J. Risselada, T. Salditt, S. J. Marrink, M. Müller, and V. Knecht. Interbilayer repulsion forces between tension-free lipid bilayers from simulation. *Soft Matter*, 9:10705–10718, 2013.
10. V. Knecht and H. Grubmüller. Mechanical coupling via the membrane fusion SNARE protein. *Biophys. J.*, 84:1527–1547, 2003.
11. M. Bowen and A. T. Brunger. Conformation of the synaptobrevin transmembrane domain. *Proc. Natl. Acad. Sci. USA*, 103:8378–8383, 2006.
12. J. Han, K. Pluhackova, D. Bruns, and R. A. Böckmann. Synaptobrevin transmembrane domain determines the structure and dynamics of the SNARE motif and the linker region. *Biochim. Biophys. Acta*, 1858:855–865, 2016.
13. M. Müller, K. Katsov, and M. Schick. A new mechanism of model membrane fusion determined from Monte Carlo simulation. *Biophys. J.*, 85:1611–1623, 2003.
14. K. Katsov, M. Müller, and M. Schick. Field theoretic study of bilayer membrane fusion. Hemifusion mechanism. *Biophys. J.*, 87:3277–3290, 2004.
15. K. Ch. Daoulas and M. Müller. Exploring thermodynamic stability of the stalk fusion-intermediate with three-dimensional self-consistent field theory calculations. *Soft Matter*, 9:4097, 2013.
16. S. Aeffner, T. Reusch, B. Weinhausen, and T. Salditt. Energetics of stalk intermediates in membrane fusion are controlled by lipid composition. *Proc. Natl. Acad. Sci. USA*, 109:9678–9679, 2012.
17. D. Milovanovic, A. Honigmann, S. Koike, F. Göttfert, G. Pähler, M. Junius, S. Müllar, U. Diederichsen, A. Janshoff, H. Grubmüller, H. J. Risselada, C. Eggeling, S. W. Hell, G. van den Bogaart, and R. Jahn. Hydrophobic mismatch sorts SNARE proteins into distinct membrane domains. *Nature Communications*, 6:5984, 2015.
18. H.J. Risselada, A.E. Mark, and S.J. Marrink. Application of mean field boundary potentials in simulation of lipid vesicles. *J. Phys. Chem. B*, 112:7438–7447, 2008.
19. M. Müller, K. Katsov, and M. Schick. New mechanism of membrane fusion. *J. Chem. Phys.*, 116:2342–2345, 2002.
20. K. Katsov, M. Müller, and M. Schick. Field theoretic study of bilayer membrane fusion. Mechanism of a stalk-hole complex. *Biophys. J.*, 90:915–926, 2006.
21. H. J. Risselada, G. Marelli, M. Fuhrmans, Y. G. Smirnova, H. Grubmüller, S. J. Marrink, and Marcus Müller. Line-tension controlled mechanism for influenza fusion. *PLoS ONE*, 7:e8302, 2012.
22. H. J. Risselada, G. Bubnis, and H. Grubmüller. Expansion of the fusion stalk and its implication for biological membrane fusion. *Proc. Natl. Acad. Sci. USA*, 111:11043–11048, 2014.